

PAPER

# Electrical and optical characterization of quantum dots PbS/TiO<sub>2</sub> based heterojunction as a SWIR detector and a proposed design of PbS/TiO<sub>2</sub>-PeLED as a SWIR to visible upconversion device

To cite this article: Elad Hechster *et al* 2019 *Mater. Res. Express* **6** 066210

View the [article online](#) for updates and enhancements.



**IOP | ebooks™**

Bringing you innovative digital publishing with leading voices to create your essential collection of books in STEM research.

Start exploring the collection - download the first chapter of every title for free.



## PAPER

# Electrical and optical characterization of quantum dots PbS/TiO<sub>2</sub> based heterojunction as a SWIR detector and a proposed design of PbS/TiO<sub>2</sub>-PeLED as a SWIR to visible upconversion device

RECEIVED  
20 September 2018REVISED  
11 February 2019ACCEPTED FOR PUBLICATION  
14 March 2019PUBLISHED  
29 March 2019Elad Hechster<sup>1</sup>, Daniel Amgar<sup>2</sup>, Neta Arad-Vosk<sup>3</sup>, Tal Binyamin<sup>2</sup>, Amir Sa'ar<sup>3</sup> , Lioz Etgar<sup>2</sup> and Gabby Sarusi<sup>1</sup> <sup>1</sup> Electro-Optics Engineering Unit and Ilse Katz Institute for Nanoscale Science and Technology, Ben-Gurion University of the Negev, Beer-Sheva, 8410501 Israel<sup>2</sup> Institute of Chemistry, Casaly Center for Applied Chemistry, The Hebrew University of Jerusalem, Jerusalem 91904, Israel<sup>3</sup> Racah Institute of Physics and the Harvey M. Kruger Family Center for Nanoscience and Nanotechnology, the Hebrew University of Jerusalem, Jerusalem 91904, IsraelE-mail: [sarusiga@bgu.ac.il](mailto:sarusiga@bgu.ac.il)**Keywords:** colloidal quantum dots, SWIR to visible upconversion device, PbS quantum dots, TiO<sub>2</sub>/PbS(QD) heterojunction, PbS perovskite LED structure

## Abstract

In this work we present the electrical and optical characterizations of a Short Wavelength Infrared (SWIR) photodetector, which consists of tandem FTO/TiO<sub>2</sub>/PbS colloidal quantum dot (CQD) layers. The TiO<sub>2</sub>/PbS hetero-structure can be operated either as a standalone detector or as the SWIR absorption section of a SWIR to visible up-conversion device (SWVUCD) when visible photo-emission layer is attached to infrared absorption layer such as this heterojunction. The results reveal the existence of the PbS CQD's bandgap operating in the SWIR spectral range as well as exhibit mixed photovoltaic and photoconductive characteristics. The optical characteristics of the different grown layers were analyzed by photoluminescence and absorption methods. The current density—voltage (J–V) curve at forward bias shows a crossover effect, however, no rollover effect has been observed. The latter indicates that there is no Schottky barrier component in this structure. We have concluded that in our case the energy bandgap of the PbS CQD is 0.93 eV where a defects states level with energy of 0.83 eV in the bandgap is evident. Finally, we propose and discuss a possible architecture of such a SWIR photosensitive hetero-structure wafer bonded to a Perovskite LED in order to form an imaging SWVUCD. Such a SWVUCD, when attached to a visible CMOS sensor, can serve as a low cost SWIR based detector for eye-safe Laser Imaging Radar (LiDAR) and for SWIR night vision applications. Such an architecture is favorable over current technologies with regard to manufacturing costs, preparation complexity, power consumption, size and weight.

## 1. Introduction

The Short Wavelength Infrared (SWIR) spectral range (1–2.5 μm) [1] is of great interest as fog and smoke penetrating wavelengths for sensors in the automotive industries and especially for autonomous car [2]. In some cases, such sensors can also be used for eye-safe Laser Imaging Radar (LiDAR) systems [3] and Night Vision Devices (NVD) [4] due to their ability to propagate in adverse atmospheric conditions. This is owing to the relatively long wavelength compared to the visible range, alongside the ability to yield good quality images. In addition, in this spectral band, the bandgap of the photo-sensitive layer is still relatively wide (around 0.8 eV), which enables its operation at room temperatures [5]. A SWIR to Visible Up-Conversion Device (SWVUCD) is a device that up-converts a SWIR image into a visible image through an optical-electrical-optical process, while maintaining the image spatial information throughout this process [6]. A SWVUCD may, under certain conditions, function as a NVD that also utilizes the natural SWIR radiance (air glow), provided that its noise level

is very low [1, 2], but in most cases artificial illumination may still be needed. During the last few decades, various device architectures were proposed for SWVUCD that were based on infrared light absorption in semiconductors (InGaAs) or on blue shifted nano-structure based layers (such as PbS or PbSe), where the visible emission layer could be a semiconductor based LED or an organic material such as an OLED [1, 3–11] and liquid crystals [7].

Pb-Chalcogenides in general are attractive materials for use as the photo sensitizing layer of infrared detectors. They exhibit high mobility and low electron and hole effective masses. Their large exciton Bohr radius enables the study of the strong confinement regime of their quantum structure up to relatively large sizes [8]. Utilizing their quantum size effect yielded numerous applications in different systems, including infrared lasers and detectors [9], biological markers, photovoltaic (PV) solar cells [10–12], Q-switches, nano-electronic devices and the detection layer of infrared to visible up-conversion devices (UCDs) [13].

The use of Pb-Chalcogenides in the form of Colloidal Quantum Dots (CQDs) for detection applications makes it possible to tailor their bandgap, and thus their spectral response [14]. Moreover, their preparation is done in regular laboratory hoods without the need for a cleanroom environment and ultra-high vacuum systems [10, 12], as opposed to epitaxial grown InGaAs/InP compounds that use MBE or MOCVD epitaxial growth methods. Furthermore, the photon to photon conversion efficiency of the latter, when integrated with an OLED to form a SWVUCD, found to be only 0.25% [15], while in the case of PbSe it was 1.3% [16]. In addition, PbS nano-structure based layers exhibit high absorption coefficients, thanks to their relatively high oscillator strength that is pronounced in the 3D quantum confinement of the quantized particles [15]. Therefore, a layer of a few hundreds of nano meters thick made of CQDs can absorb most of the incoming photons, while for the bulk semiconductors several micrometers in thickness is required. For a SWVUCD, it is crucial to have very thin absorption layer, the thinner the layer is, the less is the blurring of the visible image, due to the inherent lateral diffusion of the photo-excited carriers when they are drifted towards the visible emission layer.

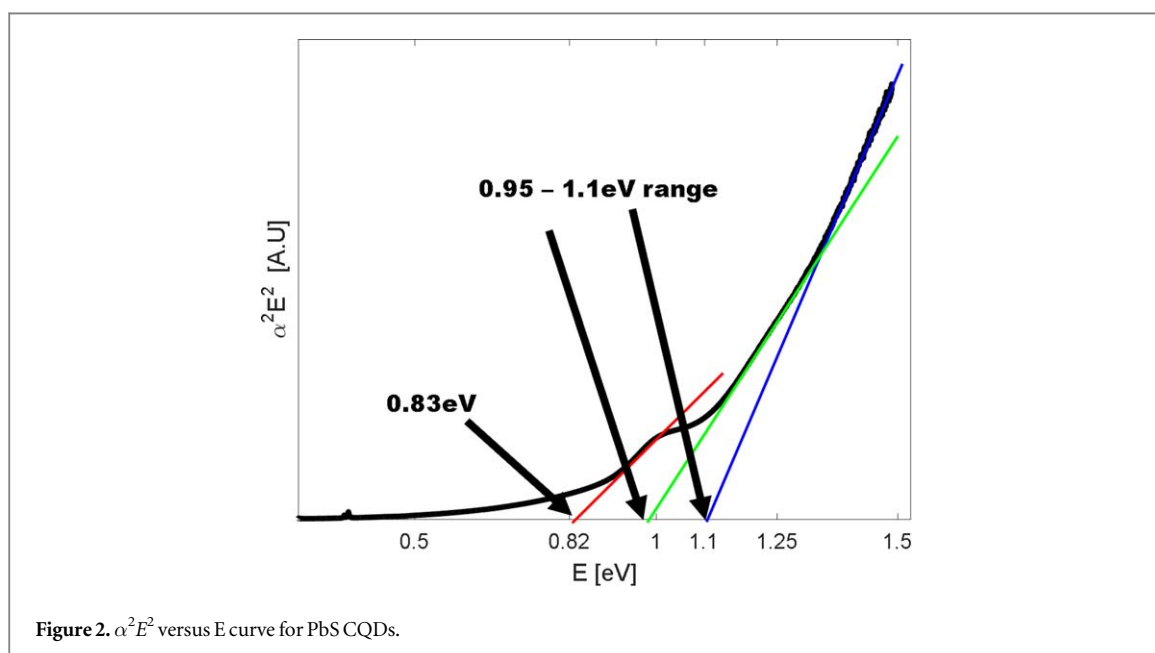
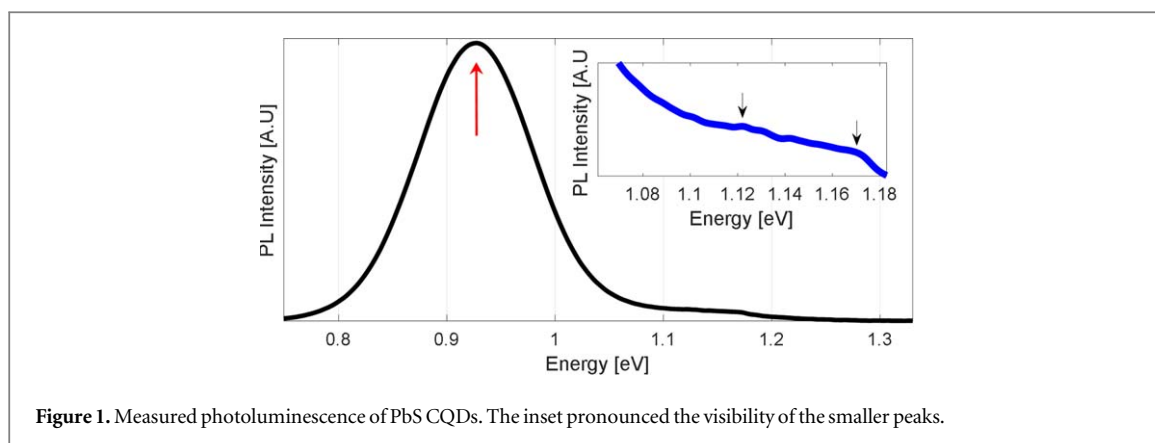
With respect to the SWVUCD: it is desirable to utilize a visible light emitter that does not require a cleanroom and other procedures for its fabrication. The most common device for that purpose is the OLED [1, 4–7, 10, 17]. D Y Kim *et al* reported the realization of an UCD having PbSe CQDs used as the light sensor, together with an OLED as the visible light emitter [16]. In recent years, extensive work has been done related to Perovskite LEDs (PeLEDs), owing to the combination of the low-cost processing of the semiconducting materials with favorable optoelectronic properties. Among these are: strong absorption coefficients, tunable bandgap, large and balanced electron and hole mobility, long carrier diffusion lengths, small exciton binding energy and unique defect properties with only shallow point defects [17–21]. Undeniably, PeLEDs are attractive as alternative emitters that can overcome the disadvantages of OLEDs, such as better current efficiency at room temperature [22]. Therefore, possible hybridization of a SWIR sensitizing layer of Pb-Chalcogenides CQDs with a PeLED could be a pioneering solution for new SWVUCD structure design. Such an architecture will be discussed herein.

In this paper we study the optical and electrical properties of a SWIR sensitive hetero-structure. The hetero-structure is composed of a tandem Titanium Oxide ( $\text{TiO}_2$ ) hole blocking layer and a PbS CQDs photo-sensitizing layer, which are deposited onto a commercial Fluorine-doped Tin Oxide (FTO) capped glass. Analysis of the results demonstrates a combination of both PV and photoconductive (PC) characteristics and, inherently, explains the spectral response. Based on the measured parameters of this hetero-structure and the published parameter of PeLED, we propose a model and discuss a novel design concept of a SWVUCD architecture that is a hybridization between the SWIR hetero-structure and a PeLED.

## 2. Experimental study

### 2.1. Synthesis of PbS QDs

In a typical synthesis, the lead oleate precursor is prepared inside a nitrogen-filled glove box by combining 0.27 g of lead oxide ( $\text{PbO}$ ,  $\geq 99.9\%$ , Sigma-Aldrich) with 0.75 ml of oleic acid (OA, 90%, Sigma-Aldrich) in a molar ratio of 1:2 in a three-necked-flask. The latter requires stirring. The flask is connected to a Schlenk line system and degassed under vacuum which is held below a pressure of 0.5 torr for 1 h at 150 °C. During this stage, any water vestiges are boiled out and the  $\text{PbO}$  dissolves, yielding a clear, light orange solution. After one hour, the temperature is raised to 180 °C and a solution of 126  $\mu\text{l}$  of hexamethyldisilathiane (TMS, synthesis grade, Sigma-Aldrich) in 6 ml of octadecene (ODE, 90%, Sigma-Aldrich) is rapidly injected into the flask under argon and stirring. Nucleation occurs immediately, observable by a color change to dark brown. Injection of the room temperature sulfur precursor decreases the flask temperature down to 150 °C. The reaction mixture is slowly reheated and stabilized at a target temperature for particle growth (180 °C in this case) and then the dispersion is taken out by syringe without any filter. The PbS QDs are precipitated with acetone by centrifuge several times and dispersed in hexane for further characterization. The expected size and bandgap of the QDs, for the desired



spectral absorption, were calculated through the Hyperbolic model and are 6.5 nm and 0.93 eV, respectively. The size distribution can be estimated from the PL measurements, the FWHM of the PL is 140 nm which suggests on a narrow size distribution. The error in the band gap calculation is very small due to the fact that it is calculated using Tauc plot which takes into account the reflectance and the transmittance of the film measured in an integrating sphere. This data is presented in figures 1 and 2.

## 2.2. PbS CQDs/TiO<sub>2</sub> hetero-structure fabrication

TiO<sub>2</sub> nanoparticles (20 nm, dyesol) were diluted at a 1:4 ratio in ethanol absolute (Sigma-Aldrich) and spin coated (5000 rpm, 30 s) onto a substrate made of SnO<sub>2</sub>:F (FTO) conductive glass (15  $\Omega\text{cm}^{-1}$ , Pilkington) coated by a layer of compact TiO<sub>2</sub> (TiDIP, 75% in isopropanol Aldrich). The substrate was then treated with TiCl<sub>4</sub>. The TiCl<sub>4</sub> concentration is 0.22 M, the electrodes are dipped in a 146 ml of this solution. A ligand exchange process from OA to 3-mercaptopropionic acid (MPA,  $\geq 99\%$ , Sigma-Aldrich) was held during the QDs' deposition as follows; a 50 mg ml<sup>-1</sup> dispersion of PbS QDs in octane (anhydrous,  $\geq 99\%$ , Sigma-Aldrich) was spin coated onto the substrate (2500 rpm, 10 s). Then, a solution of MPA in methanol (1:9) was spin coated (2500 rpm, 5 s) on the substrate to replace the OA ligands. Finally, octane was spin coated (2500 rpm, 10 s) twice to wash unconnected ligands. The number of cycles varied to receive different thicknesses of QDs layers. In total, 8 layers of PbS QDs were deposited. The thickness of the PbS QDs film is around 300 nm (we assume that in each cycle of deposition we have around 2–3 layers of QDs) based on our previous publication where we analyzed the dependence of the film thickness as a function of the number of the layers [12].

**Table 1.** Summary of the energies extracted by PL, Tauc plot and photo-response methods.

	PL	Tauc plot	Photo-response
A.		0.83 eV	$0.83 \pm 0.05$ eV
B.	$0.927 \pm 0.04$ eV	0.95–1.1 eV	$0.96 \pm 0.05$ eV
C.	$1.122 \pm 0.002$ eV		$1.15 \pm 0.05$ eV
D.	$1.17 \pm 0.002$ eV		$1.22 \pm 0.05$ eV

### 2.3. Characterization

Photoluminescence (PL) measurements were carried out using a Bruker V80 FTIR system. The PL signals were obtained by photoexcitation using a 785 nm/100 mW semiconductor laser and was detected using an InGaAs detector.

The same FTIR was used to measure the transmission ( $T$ ), where the absorption coefficient was extracted by the relation  $\alpha \equiv -\log(T)/(film\ thickness)$ .

The current-voltage measurement was performed using a 2410 Keithley source measurement unit and a tungsten lamp (700–2500 nm) filtered by a Si double-side polished wafer, to filter out the wavelengths under 1100 nm.

The photo-response measurements were performed in a setup similar to that reported in reference [9] where the hetero-structure was placed externally to the FTIR and illuminated by the tungsten lamp. In this setup the hetero-structure is used as the photo-detector of the FTIR. This consequently generated photocurrent that was amplified by a low-noise current preamplifier (SRS model SR570). The preamplifier also biases the hetero-structure.

## 3. Results and discussion

### 3.1. Optical measurements

Previous works employed PbS CQDs in solar-cells [15, 16, 18, 23]. PbS CQDs were prepared similarly to the procedure reported by Hines, Margaret A *et al* [14]. Yet, the bandgap of the PbS CQDs in our case was tailored to absorb in the SWIR spectral band.

Figure 1 shows the normalized photoluminescence (PL) of the PbS CQDs based layer deposited directly on glass.

As can be seen from figure 1, the CQDs have a main peak at  $(0.927 \pm 0.04)$ eV, which verifies their bandgap in the SWIR spectral range and, using the Hyperbolic model, fits to particles sizes of 6.5 nm. The full width half maximum (FWHM) is about 0.12 eV, which directly correlated to their CQDs size distribution. Additional smaller peaks are observed at energies of  $(1.122 \pm 0.002)$ eV and  $(1.7 \pm 0.002)$ eV. Although in first glance these picks are barely visible, their existence will later be verified by other measurements techniques as shown herein. However, the other nearby peaks in the inset, although have almost the same weight, were not investigated as they have not seen in the measurements and could not be verified.

Next, the PbS CQDs optical transmission,  $T$ , was measured and the absorption coefficient,  $\alpha \equiv -\log(T)/(film\ thickness)$ , was calculated. We normalized  $\alpha$  so that  $film\ thickness = 1$ , since we only wanted to investigate the specific energies at which absorption occurs rather than what is the  $\alpha$  values for these energies. Figure 2 shows the Tauc plot of  $\alpha^2 E^2$  versus the photon energy  $E$  from which the bandgap of the quantum dots was extracted [9].

As can be seen from figure 2, there are three observable tangents that intersect with the  $x$ -axis to define the PbS CQDs excitation states. The red line is linearly fitted to one part of the graph and defines one excitation state. The green and blue lines refer to another part of the graph and determine the energy ranges inside which other excitation states are located. The intersection values are summarized in table 1 herein. A deep interpretation of these values and the two regions are given there. Note that we could not see if there is another plateau and linear region beyond 1.5 eV, due to our system limitation. In addition, the peak below 0.5 eV could be attributed to noises as it is 10-fold smaller than the peak located around 1 eV.

### 3.2. Electrical measurements

In order to enhance the photo-conductivity of the QD PbS layer, the OA ligands in the PbS CQDs solution were exchanged with 3-mercaptopropionic (MPA) according to the procedure presented in the experimental section [24]. In this process, the conductivity of the PbS CQDs sensitizing layer is enhanced by reducing the interspace between neighboring PbS CQDs from  $\sim 1.5$  nm to  $\sim 0.9$  nm [25].

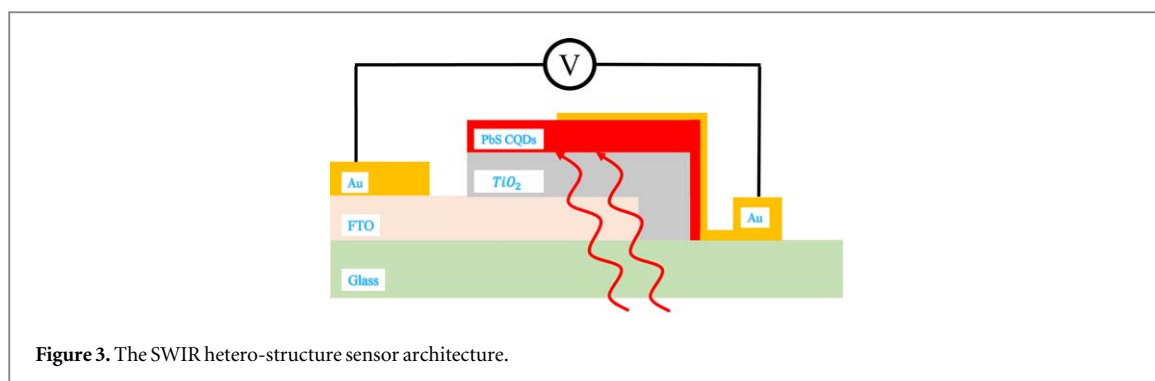


Figure 3. The SWIR hetero-structure sensor architecture.

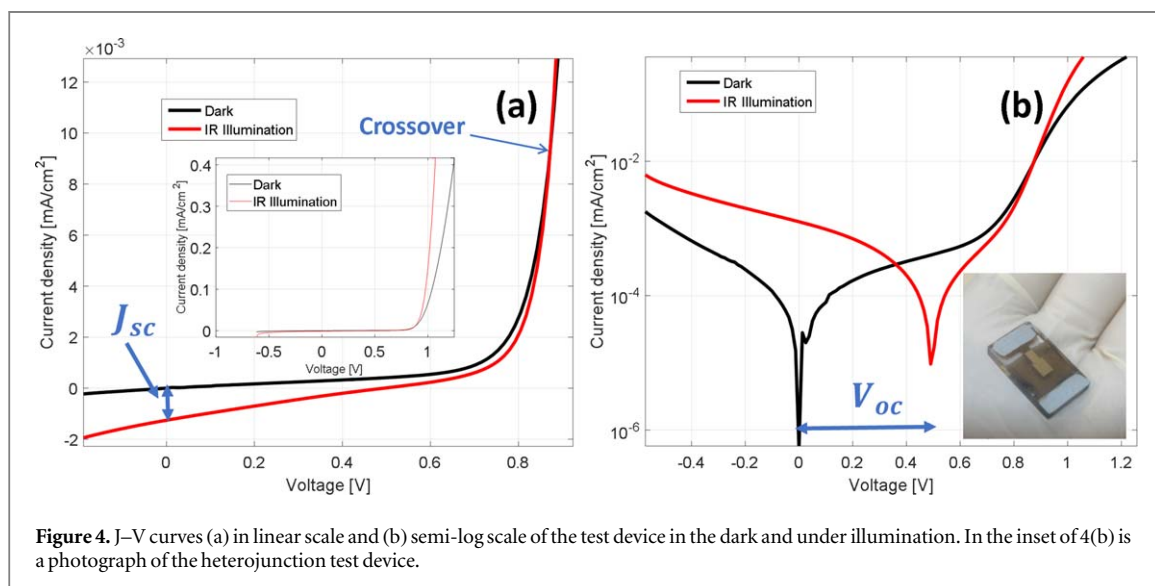


Figure 4. J–V curves (a) in linear scale and (b) semi-log scale of the test device in the dark and under illumination. In the inset of 4(b) is a photograph of the heterojunction test device.

Figure 3 illustrates the layers stack of the tested SWIR heterojunction sensor (the aspect ratio are not to scale). On the FTO capped glass are tandem layers of  $\text{TiO}_2$  and PbS CQDs, topped with Au electrodes. The electrodes are evaporated using a shadow mask that defines the active area. The device is biased via the electrodes, the FTO and the top PbS CQDs layers.

Current-voltage characteristics of the SWIR sensor were measured in dark and under SWIR illumination. Figures 4(a) and (b) present the linear and semi-log current density versus voltage (J–V) characteristics of the tested sample, respectively. A photograph of the sample is shown at the inset of figure (b). The effective Au electrode area, evaporated on the PbS CQDs layer, is  $0.12 \text{ cm}^2$ , and the silver paste strips are attached onto the Au electrodes on either edge of the sample.

The effect of illumination on the J–V curves can be seen in both the linear and the semi-log plots of figure 4. The short circuit current ( $J_{sc}$ ) and the open circuit voltage ( $V_{oc}$ ) were measured to be  $(1.26 \pm 0.2) \times 10^{-3} \text{ mA/cm}^2$  and  $(0.5 \pm 0.01) \text{ V}$ , respectively. These results demonstrate that both PV and PC effects are dominant at negative bias and both contribute to the photocurrent.

As can be seen in figure 4(a), we have a crossover effect (intersection of dark and photocurrent curves under forward bias) at 0.87 V; this crossover may be related to the built-in voltage within the device [23]. However, no rollover effect (current saturation at high forward bias) under illumination occurred (see the inset of figure 4(a)). Hence, we can infer that there is no Schottky barrier at the PbS CQDs/Au interface [26]. Another strengthening argument that there is no Schottky barrier can be noticed when comparing the PL peak in figure 1 and the  $V_{oc}$  in figure 4. The maximum  $V_{oc}$  obtainable in a Schottky geometry is probably limited to  $E_g/2q$ , where  $E_g$  is the bandgap. However, in our case  $V_{oc} > \frac{E_g}{2q}$  ( $\frac{E_g}{2} \sim 0.46 \text{ eV}$ ), which is above this limit [26]. Notice the inset, where the slope of J is steeper under illumination than that in dark. This is thanks to the photocurrent-density attribution that is added to the dark current-density. As for the peak shown by the black curve in figure 4(b), it is attributed to traps; the bias increases gradually from zero until it reaches a value that enables the trapped charge carriers to release, what causes the line to break abruptly rather than increases smoothly.

To further study the origin of the combined PV and PC effects, we used Fourier-Transform Photocurrent Spectroscopy [14, 27] to measure the relative spectral response of the heterojunction device. For this

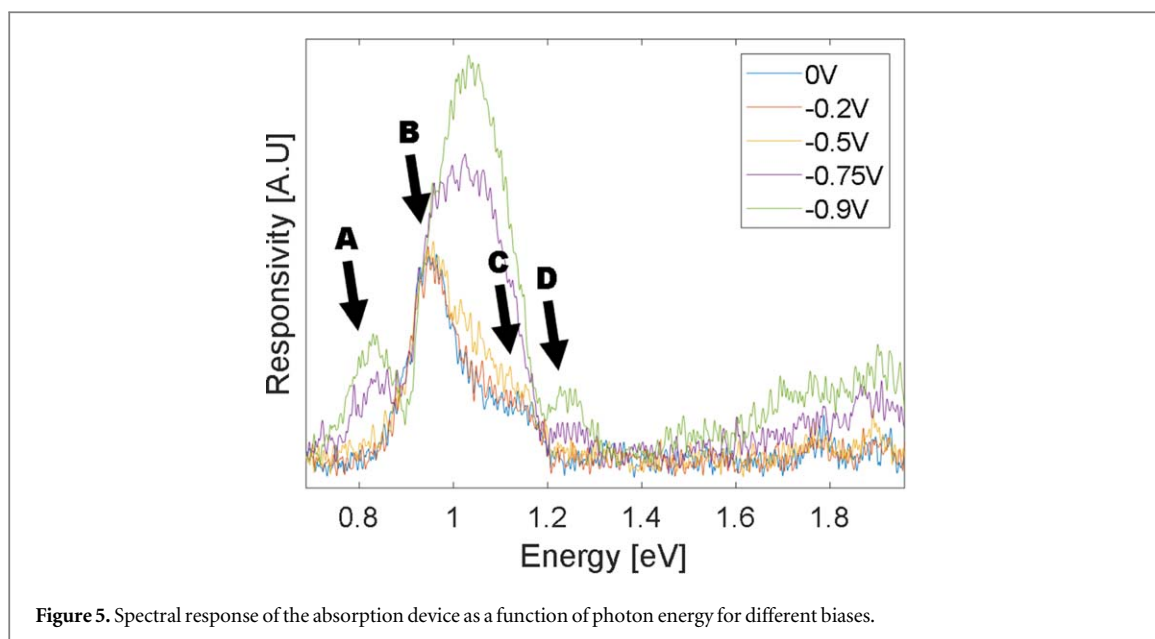


Figure 5. Spectral response of the absorption device as a function of photon energy for different biases.

measurement, our detector was used as the detection section of the FTIR, bypassing the original FTIR detector. The generated photocurrent was amplified by a low-noise current preamplifier. Figure 5 shows the spectral photo-response curves for different reverse bias.

Evidently, from 0 V to  $-0.5$  V there are two peaks, at  $(0.96 \pm 0.05)$  eV and  $(1.15 \pm 0.05)$  eV (B and C in figure 5), which unite and averaged to one peak for higher bias. These peaks can be attributed to the PV effect, since they appear at 0 V bias as well. However, for negative bias that is greater than  $-0.5$  V, two more peaks are evident, at  $(0.83 \pm 0.05)$  eV and  $(1.22 \pm 0.05)$  eV (A and D in figure 5). Since these peaks do not appear at lower bias, we can associate them with the PC contribution. Similarly, when approaching higher photon energies one can see that the photo-response increases with bias thanks to the greater electromotive force which enhances the drift current. Nevertheless, we could not define the peaks' locations for these high energies due to the limitations of our system.

Table 1 summarizes the energies extracted by the different methods, PL, Tauc plot on the absorption spectrum and the photo-response.

We can see that the energy values obtained by the three different methods are in good agreement and within a reasonable error range. When considering the PL energies of rows B, C and D, we can see that the energies presented in the PL column are lower than their associated energies obtained by the Tauc plot method and by the photo-response. The latter findings can be attributed to the Stokes shift, which means that the energy state to which electrons are excited by photons is higher than the energy state from which electrons recombined with holes in the valence band [13]. When comparing the PL and the photo-response we can see that the Stokes shifts are  $\sim 0.03$  eV,  $\sim 0.03$  eV and  $\sim 0.05$  eV for rows B, C and D, respectively.

Let us now explore the origins of each of the peaks in table 1. Referring to row A in table 1, for the PL result, which reflects the emission peaks, the peak at 0.83 eV is not observed. Yet, this peak is observed in the Tauc plot and in the photo-response results, which are associated with absorption. Therefore, we associate this peak to defect states within the semiconductor material, which indicate an imperfection of the material and are likely to absorb photons, but less likely to go through a radiative process and emit photons. The ratio between the defect states density and the highest peak's states density is 1:4 and may influence the electrical performances of the device. Considering figure 5, we see that this peak arises when the biases are higher than  $-0.75$  V. This is because of the photo-excited charge carriers that are trapped in defect states are less likely to be ejected, but with sufficient bias, they are pulled out of the traps and thus contribute to the total photocurrent. The peak distribution shown in rows B, C and D, however, can be attributed to 3 different CQD populations. In order to prevent confusion and see the full energy picture of our PbS CQDs, figure 6 schematically summarizes the bandgap alignment and indicates the energy levels described above, i.e. the bandgaps of the three populations and the defect state.

As can be seen in figure 5, the peaks become more pronounced as the bias increases. This can be explained by the fact that the lifetime of PbS CQDs excited carriers increases with their size, due to the decreasing bandgap [28]. Thus, the mean free path of the photo-excited charge carriers, originating from smaller PbS CQDs, is shorter and, hence, less likely to contribute to the photocurrent. By increasing the bias on the sample, these charge carriers are drifted out and contribute to the photocurrent.

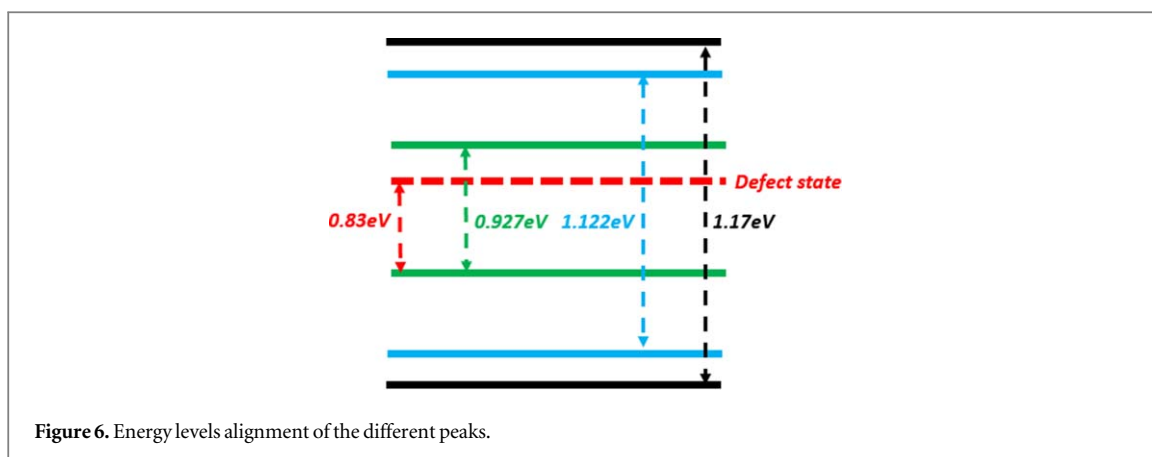


Figure 6. Energy levels alignment of the different peaks.

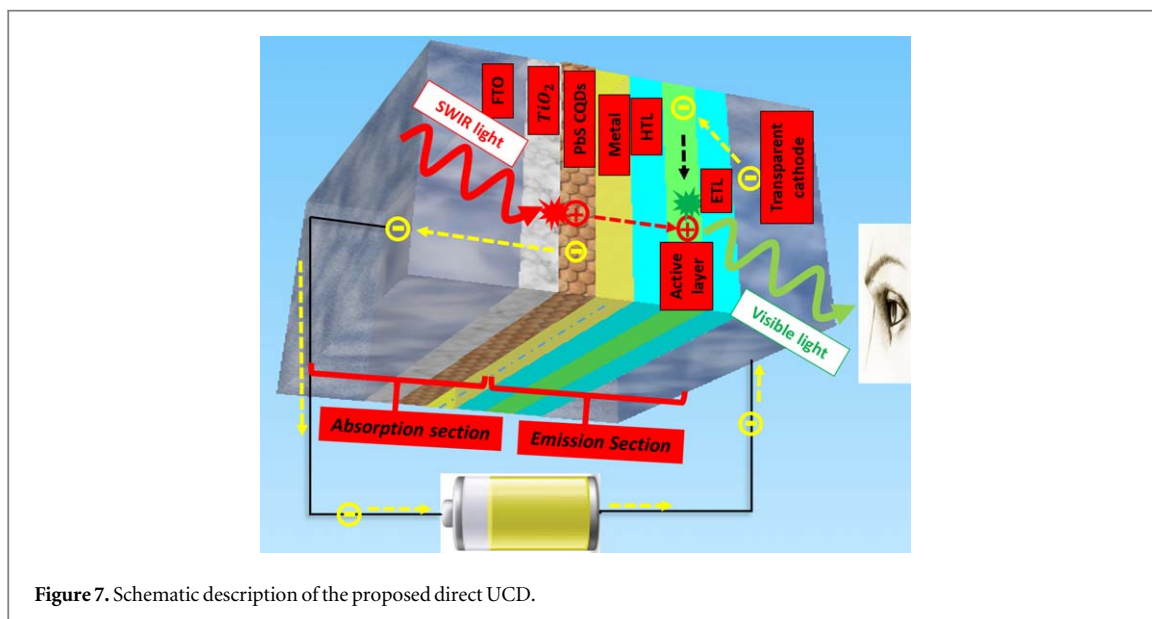


Figure 7. Schematic description of the proposed direct UCD.

### 3.3. Possible hybridization with PeLED to be used for upconversion device

As mentioned above, the SWIR sensor presented in figure 3 can serve as the SWIR detection layer of a SWVUCD. This can be realized only when the latter is integrated with a visible light emitter such that the hetero-structure operates in forward bias with respect to the visible light emitter. The concern of non-zero dark current of the SWIR sensor in forward bias is removed, thanks to the fact that light emitters usually operate in high current densities of a few  $\text{mA}/\text{cm}^2$ . Considering the inset of figure 4(a), since the SWIR sensor and the visible light emitter are in series, if the bias applied to the SWIR sensor is such that the dark current is just below the threshold current to light the visible light emitter, so the emission section will not be active in such condition. In this way the SWVUCD operates only when SWIR light is absorbed and generates photocurrent in addition to the dark current.

Now, let us propose an architecture of a SWIR detector and PeLED hybridization in order to form a direct SWVUCD. The SWVUCD is made of two sections that are wafer bonded to one another, in our case: (1) the SWIR sensitive hetero-structured absorption section; and (2) the PeLED emission section. The overall architecture and the imaging principle of the SWVUCD, is presented in figure 7.

The SWIR image is projected using fore optics through the FTO transparent anode, the  $\text{TiO}_2$  transparent hole blocking layer and is absorbed in the PbS CQD photosensitizing layer. Photo-excited electron-hole pairs are generated and separated by the external applied electric field. The holes are drifted towards the PeLED and thereby preserve the image spatial information. Simultaneously, the electrons are drifted towards the anode and injected by the battery through the transparent cathode deposited on the top of the PeLED, where the electron-hole pairs are recombined. As a result, there is an emission of visible photons that are spatially correlated with the SWIR image through the transparent cathode that can be collimated to the observer's eye or can be attached to a CMOS sensor focal plane array to generate a visible image. The spatial information of the image is preserved

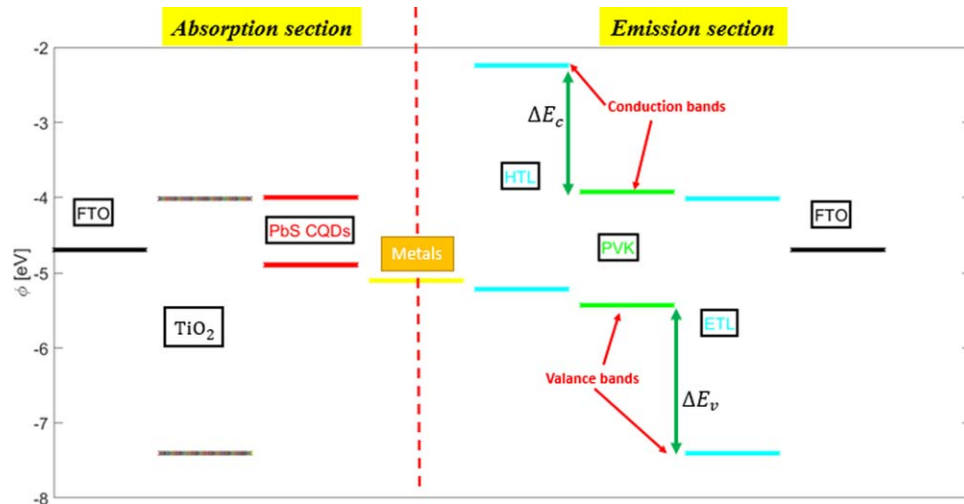


Figure 8. Electronic energy band structure of the proposed SWVUCD.

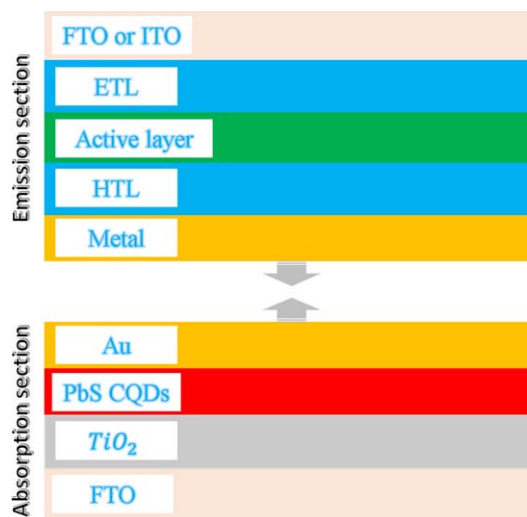


Figure 9. Wafer bonding of the absorption section and the PeLED device (top).

thanks to the thin layers of SWIR absorber and visible emitter that are only a few hundreds of nanometers thick. Figure 8 shows the energy band alignment structure of the proposed hybridized device.

The device structure can be divided into two sections: a SWIR absorption section and the visible emission section, where each has its own function. As can be seen in figure 8, the Perovskite (PVK) layer is sandwiched between the hole transparent layer (HTL) and the electron transparent layer (ETL). The energy difference  $\Delta E_c$  that exists between the HTL and PVK layers blocks the electrons. Similarly, the energy difference  $\Delta E_v$  between the ETL and PVK layers blocks the holes. As a result, the charge carriers are electrically confined, and a radiative recombination is further enhanced.

Basically, it is more complex to fabricate the proposed SWVUCD sequentially. For this reason, the absorption and emission sections are preferably grown separately and then bonded together from their metal sides to form the SWVUCD, as illustrated in figure 9. The bonding of the metals can be done by different methods described in the literature [27, 29, 30]. The best way to bond them depends on the metal of the emission section and requires further research.

The reasoning behind these separated fabrications is that each of the sections can be grown separately and operates independently. Bonding the sections enables the same operation of each section, as if it had not been connected to the other.

Notice that the conditions for this proposed SWVUCD to work properly are as follows: first, the metal layer (that serves as double sided mirror), between the two sections, has to be pixelated in order to minimize any lateral diffusion of the charge carriers and thus preserve the spatial image information. This pixelation can be

accomplished by different methods, among which are Reactive Ions Etching (RIE) and Ion Beam Milling (IBM) [13]. In the latter case, a test sample is used to extract the etch rate and dose of the etcher. Then, these two parameters are taken into consideration when the IBM is applied. Secondly, the metal layer must be very thin, down to a few tens of nanometers, to allow the holes to flow through it with minimal loss. In addition, SWIR objective optics should be placed in front of the absorption section at such a distance that the PbS CQD sensitizing layer will be at the focal plane of the objective. The PeLED should be such that its anode side will be the double-sided mirror metal and the FTO (or ITO) will be the cathode. In this case, the holes (which have been photo-generated at the PbS CQDs layer) will be drifted to the PeLED at the proper direction. For the latter condition, one alternative for the visible emission section is the PeLED reported by Yuan, Mingjian, *et al* [18], tuned to visible, which is biased positively from its metal side. In their work, they represent a PVK mixed material, comprising a series of differently quantum-size-tuned grains that funnel photo-excitations to the lowest-bandgap light-emitter in the mixture. Their device exhibits an external quantum efficiency (EQE) of 8.8% and radiance of  $80 \frac{\text{W}}{\text{sr} \cdot \text{m}^2}$ . They used ITO as the anode bottom electrode, a thin  $\text{TiO}_2$  layer as an electron injection layer, an emissive layer  $(\text{PEA}_2(\text{MA})_{n-1}\text{Pb}_n\text{I}_{3n+1})$ , a hole injecting layer poly(9, 9'-dioctylfluorene) (F8) and molybdenum trioxide ( $\text{MoO}_3$ )/gold (Au) as the top electrode. This design is coherent with the light emitter structure proposed above. Since the absorption and emission sections are sequential, their current should be equal when the SWVUCD operates. According to figure 4 in their work, their PeLED has quite high EQE for a current density of only  $\sim 5 \frac{\text{mA}}{\text{cm}^2}$ , while our hetero-structure can achieve  $\sim 7 \frac{\text{mA}}{\text{cm}^2}$  even for a reverse bias of  $-5 \text{ V}$  and all the more for forward biases, as implied in the inset of figure 4(a).

#### 4. Summary and conclusion

In this paper we investigated the optical properties, J–V characteristics and photo-response of a SWIR sensitive hetero-structure having a stack of FTO/ $\text{TiO}_2$ /PbS CQDs/Au layers. By comparing the different features, we have explained the inherent sources of each peak in the different spectral responses. We observed a crossover effect in the J–V curves, but the lack of the rollover effect led us to assume that no Schottky barrier existed in the structure. We saw that this structure exhibits combined photovoltaic and PC effects. Finally, we proposed the use of this SWIR sensor as the absorption section of a SWVUCD, combined with a PeLED for imaging applications, and described how this device should be realized.

#### Acknowledgments

The authors acknowledge the support of the Israeli National Nanotechnology Initiative - INNI for their Focal Technology Area (FTA) grant.

#### ORCID iDs

Amir Sa'ar  <https://orcid.org/0000-0003-0917-7913>

Gabby Sarusi  <https://orcid.org/0000-0001-6717-2235>

#### References

- [1] Bourlai T *et al* 2010 Cross-spectral face verification in the short wave infrared (SWIR) band *Pattern Recognition (ICPR), 2010 20th Int. Conf. on. IEEE*
- [2] Malchow D *et al* 2007 High speed short wave infrared (SWIR) imaging and range gating cameras. *Thermosense XXIX. Vol. 6541. International Society for Optics and Photonics 6541*
- [3] Rothman J *et al* 2014 High operating temperature SWIR HgCdTe APDs for remote sensing, Emerging technologies in security and defence II; and quantum-physics-based information security III. *Vol 9254. International Society for Optics and Photonics 9254*
- [4] MacDougall M *et al* 2009 Low dark current InGaAs detector arrays for night vision and astronomy *Infrared Technology and Applications XXXV. Vol 7298. International Society for Optics and Photonics 7298*
- [5] Hansen M P and Douglas Malchow S 2008 Overview of SWIR detectors, cameras, and applications *Thermosense XXX. Vol. 6939. International Society for Optics and Photonics 6939*
- [6] Hechster E and Sarusi G 2015 Design and measurements of the absorption section of an up-conversion device based on PbSe quantum-dots *Opt. Mater.* **50** 188–92
- [7] Solodar A *et al* 2016 Infrared to visible image up-conversion using optically addressed spatial light modulator utilizing liquid crystal and InGaAs photodiodes *Appl. Phys. Lett.* **108** 021103
- [8] Hechster E and Sarusi G 2017 Modeling the PbS quantum dots complex dielectric function by adjusting the Ek diagram critical points of bulk PbS *J. Appl. Phys.* **122** 024302
- [9] Arad-Vosk N *et al* 2018 Infrared photoconductivity and photovoltaic response from nanoscale domains of PbS alloyed with thorium and oxygen *Nanotechnology* **29** 11
- [10] Etgar L *et al* 2012 Light energy conversion by mesoscopic PbS quantum dots/ $\text{TiO}_2$  heterojunction solar cells *ACS Nano* **6** 3092–9

- [11] Etgar L et al 2011 Design and development of novel linker for PbS quantum dots/TiO<sub>2</sub> mesoscopic solar cell *ACS Applied Materials & Interfaces* **3** 3264–7
- [12] Etgar L et al 2012 High efficiency quantum dot heterojunction solar cell using anatase (001) TiO<sub>2</sub> nanosheets *Adv. Mater.* **24** 2202–6
- [13] Hechster E et al 2016 Optical and electrical characterizations of a single step ion beam milling mesa devices of chloride passivated PbS colloidal quantum dots based film *AIP Adv.* **6** 075117
- [14] Hines M A and Gregory D S 2003 Colloidal PbS nanocrystals with size-tunable near-infrared emission: observation of post-synthesis self-narrowing of the particle size distribution *Adv. Mater.* **15** 1844–9
- [15] Ban D et al 2007 Near-infrared to visible light optical upconversion by direct tandem integration of organic light-emitting diode and inorganic photodetector *Appl. Phys. Lett.* **90** 093108
- [16] Kim D Y et al 2011 PbSe nanocrystal-based infrared-to-visible up-conversion device *Nano Letters* **11** 2109–13
- [17] Yantara N et al 2015 Inorganic halide perovskites for efficient light-emitting diodes *The Journal of Physical Chemistry Letters* **6** 4360–4
- [18] Yuan M et al 2016 Perovskite energy funnels for efficient light-emitting diodes *Nat. Nanotechnol.* **11** 872–7
- [19] Song J et al 2015 Quantum dot light-emitting diodes based on inorganic perovskite cesium lead halides (CsPbX<sub>3</sub>) *Adv. Mater.* **27** 7162–7
- [20] Tan Z-K et al 2014 Bright light-emitting diodes based on organometal halide perovskite *Nature Nanotechnology* **9** 687–92
- [21] Xiao Z et al 2017 Efficient perovskite light-emitting diodes featuring nanometre-sized crystallites *Nat. Photon.* **11** 108–15
- [22] Cho H et al 2015 Overcoming the electroluminescence efficiency limitations of perovskite light-emitting diodes *Science* **350** 1222–5
- [23] Moore J et al 2013 The physics of V bi-related IV crossover in thin film solar cells: applications to ink deposited CZTSSe *Photovoltaic Specialists Conf. (PVSC), 2013 IEEE 39th. IEEE* (<https://doi.org/10.1109/PVSC.2013.6745146>)
- [24] Reinhart C C and Johansson E 2015 Colloidally Prepared 3-mercaptopropionic acid capped lead sulfide quantum dots *Chemistry of Materials* **27** 7313–20
- [25] Yang K et al 2010 Re-examination of characteristic FTIR spectrum of secondary layer in bilayer oleic acid-coated Fe<sub>3</sub>O<sub>4</sub> nanoparticles *Appl. Surf. Sci.* **256** 3093–7
- [26] Gao J et al 2011 Quantum dot size dependent J–V characteristics in heterojunction ZnO/PbS quantum dot solar cells *Nano Lett.* **11** 1002–8
- [27] Nakao T et al 1993 Method of bonding metals, and method and apparatus for producing semiconductor integrated circuit device using said method of bonding metals *US Patent No. 5, 188, 280*
- [28] Moreels I et al 2009 Size-dependent optical properties of colloidal PbS quantum dots *ACS Nano* **3** 3023–30
- [29] Maroni V A 1992 Method of bonding metals to ceramics *US Patent No. 5, 079, 223*
- [30] Byron JJ, Elmore W C and De Prisco Carmine F 1960 Method and apparatus employing vibratory energy for bonding metals *US Patent No. 2, 946, 119*